mathematics

MDPI

Article

Fast Method Based on Fuzzy Logic for Gaussian-Impulsive Noise Reduction in CT Medical Images

Josep Arnal *,† **and Luis Súcar** †

Departamento de Ciencia de la Computación e Inteligencia Artificial, Universidad de Alicante, Campus de San Vicente del Raspeig s/n, 03690 San Vicente del Raspeig, Spain

* Correspondence: arnal@ua.es; Tel.: +34-965903400 (ext. 2985)

† These authors contributed equally to this work.

Abstract: To remove Gaussian-impulsive mixed noise in CT medical images, a parallel filter based on fuzzy logic is applied. The used methodology is structured in two steps. A method based on a fuzzy metric is applied to remove the impulsive noise at the first step. To reduce Gaussian noise, at the second step, a fuzzy peer group filter is used on the filtered image obtained at the first step. A comparative analysis with state-of-the-art methods is performed on CT medical images using qualitative and quantitative measures evidencing the effectiveness of the proposed algorithm. The parallel method is parallelized on shared memory multiprocessors. After applying parallel computing strategies, the obtained computing times indicate that the introduced filter enables to reduce Gaussian-impulse mixed noise on CT medical images in real-time.

Keywords: CT images; fuzzy logic; fuzzy metric; medical image enhancement; mixed impulsive and Gaussian noise; noise reduction

MSC: 03B52; 94A08; 92C55; 68W10; 68T99

Citation: Arnal, J.; Súcar, L. Fast Method Based on Fuzzy Logic for Gaussian-Impulsive Noise Reduction in CT Medical Images. *Mathematics* **2022**, *10*, 3652. https://doi.org/10.3390/math10193652

Academic Editor: Krystian Jobczyk

Received: 17 August 2022
Accepted: 30 September 2022
Published: 5 October 2022

1. Introduction

Filtering algorithms, i.e., methods to remove noise, are of the utmost importance in medical image processing (e.g., Ultrasound Imaging (US), X-rays, Computer Tomography (CT), Magnetic Resonance Imaging (MRI)) since noise can deteriorate the quality of the image and affect the disease diagnosis (e.g., identifying micro-calcifications in mammograms). Additionally, noise removal methods can be utilized to enhance medical images generated using a lowered radiation dose [1,2]. This fact is particularly important in CT medical images in order to lower the X-ray exposure, since the quantity of radiation is required to be high. Although other types of noise may be present, such as the speckle noise [3], two particularly usual kinds of noise in CT medical images are the Gaussian and the impulsive noise. The Gaussian noise is originated during the acquisition procedure and the impulsive during the transmission process [4,5]. A considerable amount of methods have been proposed to remove either impulse (see, e.g., [6–14]) or Gaussian noise (see, e.g., [4,15–18]). However, not all techniques are practical when images are corrupted with Gaussian and impulsive noise simultaneously. A possible strategy to tackle this issue is to achieve two consecutive methods to reduce first impulses and then the Gaussian noise, or vice versa. However, the application of two successive filters could significantly decrease the computing efficiency, and in consequence, this strategy could not be suitable for real applications.

In [19], an efficient hybrid method for the removal of Gaussian-impulsive noise in color images was presented. The method obtained excellent results in terms of qualitative and quantitative metrics. This filter, named FRF-FPGA (Fuzzy Rank-ordered differences statistic Filter-Fuzzy Peer Group Averaging), makes use of the fuzzy peer group notion [20]. The method is structured in two stages. Firstly, a two-step procedure founded on FRF [14] is used to remove the impulses. After that, a fuzzy smoothing process founded on the

FPGA method [20] is utilized to remove the Gaussian noise. Experiments evidenced that this method obtained outstanding results when filtering color digital images compared to other state-of-the-art filters, but it has not been evaluated in the area of medical image processing. By reason of this fact, in this research we present a method based on [19] for the elimination of mixed noise in grayscale medical images.

Furthermore, because of the large dimensions of high-resolution digital images, sequential processors are not able to execute this method in real-time. Thus, experiments prove that the FRF-FPGA method obtains excellent results in filtering quality but the computation time hinders its application for real-time filtering. Currently, parallel computation is one of the most suitable techniques to achieve real-time results or to decrease the computing time in all application areas [21–24]. Additionally, as a result of the progress in cloud computing [25,26], it is feasible to execute parallel methods without many in-house resources [27].

Due to these reasons, in this research we present a new parallel method based on the algorithm presented in [19] with the objective of enhancing its computing efficiency so it can be used in real-time medical image processing.

We have implemented this parallel method on shared memory parallel computers making use of the Open Multi-Processing (OpenMP) [28,29], and we have analyzed the parallelization on multi-cores, obtaining good speed-up results. At present, multi-cores are universally accessible, so the proposed method is a feasible and effective methodology for real-time image filtering. In this study, we considered CT medical images from the Radiopaedia dataset (Case Courtesy of A. Prof Frank Gaillard, Radiopaedia.org (accessed on 16 August 2022), rID 35508) and different noisy low dose CT (LDCT) images from the 2016 NIH-AAPM-Mayo Clinic Low Dose CT Grand Challenge [30]. The filter efficiency has been analyzed making use of the following objective measures:

- When the noise-free original image is known, the measures used were the Mean Absolute Error (MAE) [4], the Peak Signal-to-Noise Ratio (PSNR) [31], the Mean Structural Similarity Index (MSSIM) [32], and the Image Enhancement Factor (IEF) [33].
- In noisy CT images obtained with low radiation doses, where the noise changes with the exposure dose and the noise-free image is not known, the measures used were the Signal-to-Noise Ratio (SNR) [34], the Contrast-to-Noise Ratio (CNR) [34], and the Equivalent Number of Looks (ENL) [34].

The proposed algorithm is compared with other competitive filters that have been applied successfully in medical image processing, including recent fuzzy techniques. The experiments show that the introduced method improves those state-of-the-art filters with respect to the mentioned metrics. Experiments show the accuracy of the introduced technique, which takes advantage of the sensitivity of the fuzzy rank-ordered differences statistic (FROD) to detect impulses and of the fuzzy logic to determine the best number of components for a peer group. The proposed parallel method has been implemented on multi-core architectures, allowing the application to be used on a wide range of devices. The computational time analysis indicates that the method is quite efficient and achieves fast execution times which enable its implementation in real-time medical image processing.

This document is organized as follows. Section 2 presents the new denoising algorithm. In Section 3, the experiments and a comparative analysis with competitive filters are described. Section 4 describes the conclusions.

2. Materials and Methods

In this section, we propose a parallel algorithm for grayscale medical images based on the FRF-FPGA method [19] initially introduced for color images. The filter design is organized as a concatenation of an impulses reduction method and a Gaussian filter.

In the subsequent paragraphs, we will describe the two steps of the method.

2.1. Impulsive Noise Removal

The filtering method is based on the fuzzy rank-ordered differences statistic [14] explained in the subsequent lines. The $FROD$ statistic is used in place of $ROAD$ due to its effectiveness in detecting impulsive noise. Let $\mathcal{F}$ be a grayscale image. Let W_x be an $n \times n$ processing window with central pixel x. Consider W_x^0 the neighbor pixels of x in the window W_x, i.e., $W_x^0 = W_x - \{x\}$. To calculate $ROAD$ [35], the distances $d_{x,x_i},\ x_i \in W_x^0$ are ascendingly ordered, generating a set of real numbers $u_j(x)$ satisfying: $u_1(x) \leq u_2(x) \leq \ldots \leq u_{n^2-1}(x)$. For a natural number α such that $0 < \alpha \leq n^2 - 1$, the $ROAD_\alpha$ represents the α rank-ordered difference, defined as [35],

$$ROAD_\alpha(x) = \sum_{j=1}^{\alpha} u_j(x).$$

$ROAD_\alpha$ denotes the global distance from pixel x to the α closest pixels. This distance is supposed to be higher for impulsive pixels than for not noisy pixels. We used the fuzzy metric M_∞ [14] to compute $d_{x,x_i},\ x_i \in W_x^0$. This metric has been shown to be particularly useful to detect impulses. It was introduced in the context of RGB images. For two RGB image pixels $\boldsymbol{x}_i, \boldsymbol{x}_j$, the fuzzy metric M_∞ is given by:

$$M_\infty(\boldsymbol{x}_i, \boldsymbol{x}_j) = \min_{k=1}^{3} \frac{\min\{\boldsymbol{x}_i(k), \boldsymbol{x}_j(k)\} + P}{\max\{\boldsymbol{x}_i(k), \boldsymbol{x}_j(k)\} + P}. \tag{1}$$

The metric M_∞ can be defined in the context of grayscale images as:

$$M_\infty(x_i, x_j) = \frac{\min\{x_i, x_j\} + P}{\max\{x_i, x_j\} + P}. \tag{2}$$

The value P in Equation (2) was set to 1024, which has been shown to be an appropriate value [36]. Sorting $d_{x,x_i} = M_\infty(x, x_i)$ in a descending order $v_1(x) \geq v_2(x) \geq \cdots \geq v_{n^2-1}(x)$, the fuzzy ROD statistic ($FROD_m$) is given by:

$$FROD_\alpha(x) = \prod_{j=1}^{\alpha} v_j(x). \tag{3}$$

The parameter α in Equation (3) is an integer such that $\alpha < n^2 - 1$. An impulsive pixel will exhibit a reduced $FROD_\alpha$ since it is not supposed to be similar to its neighbor pixels. On the other hand, non-impulsive pixels are expected to present an $FROD_\alpha$ closer to 1. $FROD_\alpha(x)$ was utilized to detect pixels that are plainly impulses or plainly non-impulsive:

- First Step: If $FROD_\alpha(x)$ is higher than a parameter th_1, then x is marked as impulse-free.
  - If $FROD_\alpha(x)$ is less than th_2, a parameter satisfying $th_2 < th_1$, x is marked as impulsive.
  - If x fulfills $th_1 \geq FROD_\alpha(x) \geq th_2$, x is not classified at this stage, and it is studied in a second stage.
- Second Step: Another parameter, th_3, is utilized. $FROD_{\alpha'}(x)$ is calculated on W_x^0, excluding the pixels previously classified as impulses, and utilizing a parameter $\alpha' < m$. If $FROD_{\alpha'}(x) > th_3$, then x is classified as non-impulsive. Otherwise, x is classified as impulse.

Once the detection process is finalized, every element classified as impulse is replaced by VMF_{out} [37] computed using the impulse-free pixels in the filtering window W_x.

2.2. Gaussian Noise Removal

The second step involves the Gaussian noise reduction procedure. At this stage, we perform a fuzzy weighted smoothing process over the components of the peer group. For this

purpose, we explain the concepts of peer group [38] and fuzzy peer group [20]. Consider for every pixel x_0 an $n \times n$ processing window W with central pixel x_0. Consider ρ a similarity metric function [4]. Utilizing this function, the pixels $x_i \in W$ are sorted in a descending order depending on their similarity to x_0, generating a set $\{x_{(0)}, x_{(1)}, \ldots, x_{(n^2-1)}\}$ fulfilling

$$\rho(x_0, x_{(0)}) \geq \rho(x_0, x_{(1)}) \geq \cdots \geq \rho(x_0, x_{(n^2-1)}),$$

where $x_{(0)} = x_0$ is the center of the window. Then, in accordance with [38], the peer group including $m+1$ components, $\mathcal{P}_m^{x_0}$, for the pixel x_0 is given by:

$$\mathcal{P}_m^{x_0} = \{x_{(0)}, x_{(1)}, \ldots, x_{(m)}\}.$$

In [20], a methodology founded on fuzzy logic is presented to determine the best number of components for a peer group. Following the definition presented in [20], the fuzzy peer group for x_0 in a window W with central pixel x_0 is given by the fuzzy set $\mathcal{FP}_{\widehat{m}}^{x_0}$ defined on the set of pixels $\{x_{(0)}, x_{(1)}, \ldots, x_{(\widehat{m})}\}$ and determined by the membership function $FP_{\widehat{m}}^{x_0} = \rho(x_0, x_{(i)})$. Then, the best number of components, represented by $\widehat{m}$, for $\mathcal{P}_m^{x_0}$ is defined as the positive integer m, $1 \leq m \leq n^2 - 1$, maximizing the certainty for the following rule:

Fuzzy Rule: The certainty of "$m \in \mathcal{N}_W$ is the best number of components of $\mathcal{P}_m^{x_0}$".

IF "$x_{(m)}$ is similar to x_0" and the accumulated similarity of $x_{(m)}$ is big THEN "certainty for m to be the best number of elements in the peer group $\mathcal{P}_m^{x_0}$ is high".

Let $C_{FR}(m)$ represent the rule certainty of m. To compute the best number $\widehat{m}$ of components, $C_{FR}(m)$ is computed for the integers $m \in \mathcal{N}_W$, and then the m, which maximizes $C_{FR}(m)$, is selected as $\widehat{m}$ for the better number of components for $\mathcal{P}_m^{x_0}$, i.e., $\widehat{m} = \arg\max_{m \in N_W} C_{FR}(m)$. The certainty for "$x_m$ is similar to x_0" is given by the function of membership C^{x_0} determined by the function of similarity:

$$C^{x_0}(x_{(i)}) = \rho(x_0, x_{(i)}),\ i, = 0, 1 \ldots, n^2 - 1.$$

The accumulated similarity function for $x_{(m)}$ is given as:

$$A^{x_0}(x_{(i)}) = \sum_{k=0}^{i} \rho(x_0, x_{(k)}),\ i \in \{0, 1, \ldots, n^2 - 1\}.$$

Thus, the certainty for "accumulated similarity of $x_{(m)}$ is large" is given by a function of membership L^{x_0} determined by:

$$L^{x_{(0)}}(x_{(i)}) = -\frac{(A^{x_0}(x_{(i)}) - 1)(A^{x_0}(x_{(i)}) - 2n^2 + 1)}{(n^2 - 1)^2}$$
$$i = 0, 1, \ldots, n^2 - 1.$$

As a conjunction operator, the t-norm product was utilized, and hence the defuzzification procedure was not required. Therefore, $C_{FR}(m) = C^{x_0}(x_{(m)}) L^{x_{(0)}}(x_{(m)})$. In the experimentation we utilized the fuzzy similarity function ρ given by

$$\rho(x_i, x_j) = e^{-\frac{|x_i - x_j|}{F_\sigma}}, \quad i, j = 0, \ldots, n^2 - 1. \tag{4}$$

In Equation (4), F_σ is a parameter studied in Section 3. This function has been selected in view of the fact that it is a fuzzy metric according to definition presented in [39], and it has been shown to be convenient in the topic of fuzzy image filtering [9,20,40]. This similarity function ρ takes values in the interval $[0, 1]$ and fulfills $\rho(x_0, x_i) = 1$ for $x_0 = x_{(i)}$. Thus, supposing that the components of an $n \times n$ processing window W_{x_0} with central pixel x_0

are sorted in a descending order, $x_0, \ldots, x_{(n^2-1)}$, by their similarity to x_0, the filtered pixel x_{out} replacing the central pixel x_0 is given by:

$$x_{\text{out}} = \frac{\sum_{j=0}^{\hat{m}} w_j x_{(j)}}{\sum_{j=0}^{\hat{m}} w_j}, \tag{5}$$

where $w_j = \rho(x_0, x_{(j)})$. The average process in Equation (5) is calculated utilizing only the peer group components, and hence, uniquely similar pixels are utilized.

2.3. Parallel Fuzzy Filter

To reduce the computing times, a parallel method based on the described algorithm is introduced. In order to distribute the pixels of the medical image among the computing units in the parallel computer, the domain Ω of the image is split in P subdomains $\Omega_i, i = 1, \ldots P$, being P the amount of computing units. This decomposition fulfills

$$\Omega_i \subset \Omega,$$
$$\bigcup_{i=1,2,\ldots,P} \Omega_i = \Omega,$$
$$\text{and } \Omega_i \cap \Omega_j = \emptyset \text{ for } i \neq j.$$

Figure 1 exemplifies the subdomains utilized in the experimentation.

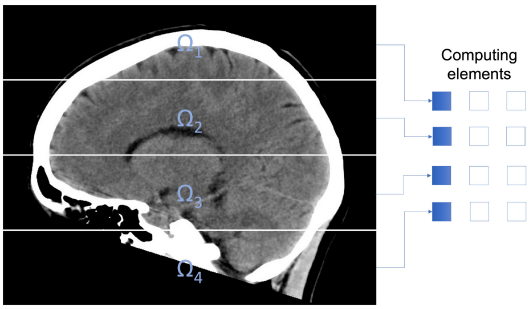

Figure 1. CT image decomposition using 4 subdomains.

To filter pixels located in the internal frontier of the subdomains, every computation unit requires of some extra pixels. Therefore, we establish an overlapping domain decomposition. Figure 2 shows an overlapping domain decomposition using four subdomains. To describe the overlap, we consider Ω_i^λ, $i = 1, ..., P$; an expansion of Ω_i, being λ a natural number defining the proportions of the overlapping area. Computation unit k filters pixels in subdomain Ω_k, but utilizing pixels in subdomain Ω_k^λ. λ is the integer part of the number $n/2$, being $n \times n$ the dimensions of the processing window.

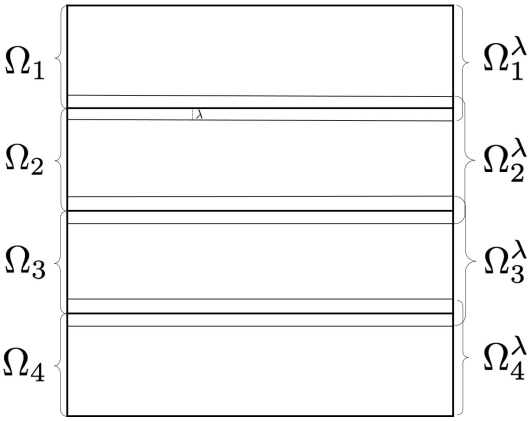

Figure 2. Overlapping domain decomposition using four subdomains.

Taking into consideration this domain decomposition, Algorithm 1 shows the parallel filtering algorithm.

Algorithm 1 Parallel Fuzzy Filter.

Require: Noisy image $\mathcal{F}$, domain decomposition $\{\mathcal{F}_{\Omega_k}\}_{k=1}^{P}$, Parameters $F_\sigma, th_1, th_2, th_3, \alpha, \alpha'$
Ensure: Denoised image.

```
for k = 1, ..., P, in parallel do
  Impulses detection: First Step

  for x in F_{Ω_k} do
    Compute: d = FROD_α(x);
    if (d > th_1) then
      x is classified as non-impulsive;
    else
      if (d < th_2) then
        x is classified as impulse;
      else
        x is classified as non-diagnosed;
      end if
    end if
  end for
  Impulses detection: Second Step

  for x in F_{Ω_k} non-diagnosed at first Step do
    Compute d = FROD_{α'}(x) excluding pixels classified as impulsive;
    if (d > th_3) then
      x is classified as non-impulsive;
    else
      x is classified as impulse;
    end if
  end for
  Impulsive Noise Removal:

  for x in F_{Ω_k} labeled as impulsive do
    x is substituted by VMF_out over noisy-free pixels;
  end for
  Gaussian Noise Removal:

  for x in F_{Ω_k} do
    Compute m̂, the better number of components in P_m^{x_0}

        x_out = (Σ_{j=0}^{m̂} ρ(x, x_(j)) x_(j)) / (Σ_{j=0}^{m̂} ρ(x_0, x_(j)))
  end for
end for
```

To study the performance of the parallel implementation, we analyze the speed-up S_P that is given by:

$$S_P = \frac{T_S}{T_P}, \tag{6}$$

where T_S is the computing time of the serial method, and T_P is the computing time of the parallel method.

3. Results

The introduced algorithm was analyzed on CT medical images from two clinical datasets. To this end, CT medical images (Figure 3) from the Radiopaedia dataset (Case Courtesy of A. Prof Frank Gaillard, Radiopaedia.org, rID 35508) were used in the experiments. These CT images appertain to a normal brain of a thirty-year-old woman. CT images were corrupted with various magnitudes of random impulsive noise (probability $p \in [0.1, 0.3]$) and Gaussian noise (standard deviation $\sigma \in [10, 30]$). For this purpose, the classical Gaussian-noise model and the random value impulsive noise [4] have been considered. The additive white Gaussian noise presents the following probability distribution:

$$p(x) = \frac{1}{(2\pi\sigma)^{\frac{1}{2}}} \exp(-\frac{x^2}{2\sigma^2}), \tag{7}$$

where σ is the standard deviation of the distribution. In the random impulsive noise model, the corrupted pixel x^* is obtained using random uniformly distributed integer values d in the interval $[0, 255]$ with probability p:

$$x^* = \begin{cases} d & \text{with probability } p, \\ x & \text{with probability } 1 - p. \end{cases} \tag{8}$$

Moreover, to show the denoising performance of the proposed method on low-dose CT images, we used different noisy low dose (quarter-dose exposure images) abdominal CT images (Figure 4) from the 2016 NIH-AAPM-Mayo Clinic Low Dose CT Grand Challenge [30].

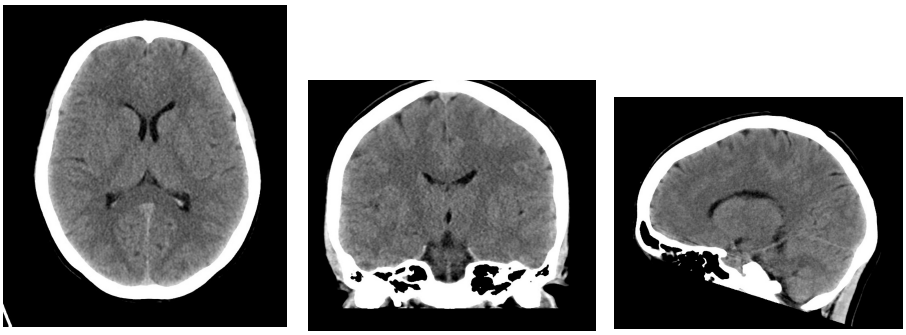

(**a**) Axial view (**b**) Coronal view (**c**) Sagittal view

Figure 3. CT medical images utilized in the experimentation. (**a**) Axial view: 1024 × 904 pixels; (**b**) Coronal view: 890 × 1024 pixels; (**c**) Sagittal view: 822 × 1024 pixels.

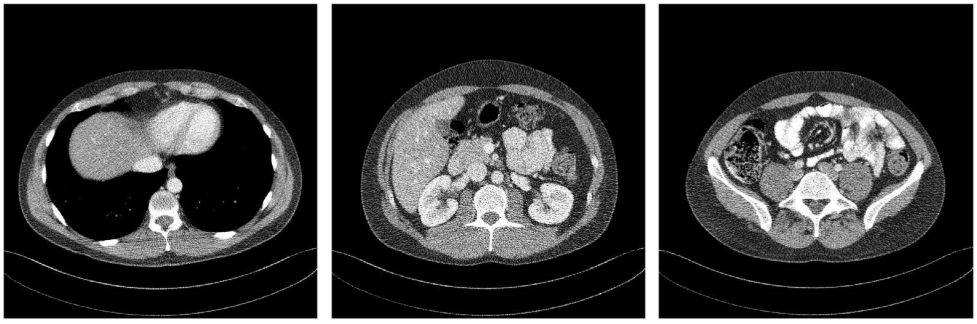

(**a**) LDCT image 1 (**b**) LDCT image 2 (**c**) LDCT image 3

Figure 4. Low-dose (quarter-dose) abdominal CT medical images, 512 × 512 pixels.

3.1. Denoising Performance

To analyze the filtering efficiency, the next metrics have been utilized. The Mean Absolute Error (MAE) [4] that estimates the detail preserving is defined as:

$$\mathrm{MAE} = \frac{1}{QMN}\sum_{k=1}^{Q}\sum_{i=1}^{MN}|o_{ik} - x_{ik}|. \tag{9}$$

The peak signal-to-noise ratio (PSNR) [31] quantifies the noise removal capacity. It is defined as:

$$\mathrm{PSNR} = 20\log_{10}\left(\frac{255}{\sqrt{\frac{1}{QMN}\sum_{k=1}^{Q}\sum_{i=1}^{MN}(o_{ik} - x_{ik})^2}}\right). \tag{10}$$

In (9) and (10), $M,\ N$ determine the image size, Q is the image channels number, x_{ik} is the k-component of the noisy or denoised pixel x_i, o_{ik} is the k-component of the original pixel o_i, and i is the position of the pixel in the image. Given two patches, $x,\ y$, of the original and denoised images, respectively, the SSIM metric between x and y is defined by [32]:

$$\mathrm{SSIM}(x,y) = \frac{(2\mu_x\mu_y + c_1)(2\sigma_{xy} + c_2)}{(\mu_x^2 + \mu_y^2 + c_1)(\sigma_x^2 + \sigma_y^2 + c_2)}, \tag{11}$$

where $\sigma_x,\ \sigma_y,\ \sigma_{xy},\ \mu_x,\ \mu_y$ are the standard deviations, covariance, and local means for $x,\ y$, and $c_1 = (K_1L)^2,\ c_2 = (K_2L)^2$ are constants utilized to make stable the division when the denominator is weak. L is a parameter representing the dynamic range of pixel values, and $K_1 = 0.01,\ K_2 = 0.03$ are constants computed experimentally [32]. To estimate the general image quality, the mean SSIM index (MSSIM) is used. The MSSIM is computed as:

$$\mathrm{MSSIM}(x,y) = \frac{1}{P}\sum_{j=1}^{P}\mathrm{SSIM}(x_j, y_j), \tag{12}$$

where $x_j,\ y_j$ are patches of the original and the noisy images, and P is the amount of patches. The MSSIM is in the interval $[0, 1]$. A greater MSSIM shows a higher preservation of structural information. The image enhancement factor (IEF) estimates general improvement and is given by [41]:

$$\mathrm{IEF} = \frac{\sum_i\sum_j(\eta_{ij} - x_{ij})^2}{\sum_i\sum_j(y_{ij} - x_{ij})^2}, \tag{13}$$

where $x_{ij}, \eta_{ij}, y_{ij}$ are the pixels of the original, the noisy, and the denoised image, respectively. To analyze the filtering efficiency in the case of the noisy low dose CT images, where there

is no noise-free reference image, the image quality metrics used were the signal-to-noise ratio (SNR) [34], the contrast-to-noise ratio (CNR) [34], and the average equivalent number of looks (ENL) [34]. The CNR measures the contrast between an image feature and an area of homogeneous noise, while the ENL measures smoothness in areas that should have a homogeneous appearance but are corrupted by noise. These image quality metrics are defined as:

$$\text{SNR} = 10 \cdot \log_{10} \frac{max(I^2)}{\sigma_n^2}, \tag{14}$$

$$\text{CNR}_m = 10 \cdot \log_{10} \frac{(\mu_m - \mu_b)}{\sqrt{\sigma_m^2 + \sigma_b^2}}, \tag{15}$$

$$\text{ENL}_m = \frac{\mu_m^2}{\sigma_m^2}, \tag{16}$$

where I is the matrix of pixel values for the CT image, and σ_n^2 is the noise variance computed on a homogeneous region. μ_m is the mean of the pixels in the mth region of interest (ROI), σ_m is standard deviation, and μ_b and σ_b are the pixel mean and standard deviation of a homogeneous region of the image, respectively. The CNR values are averaged over the red ROIs shown in Figure 5 and the ENL over the yellow homogeneous ROIs. To compute σ_b^2, the homogenous ROI in Figure 5, delimited by a dashed line, was used.

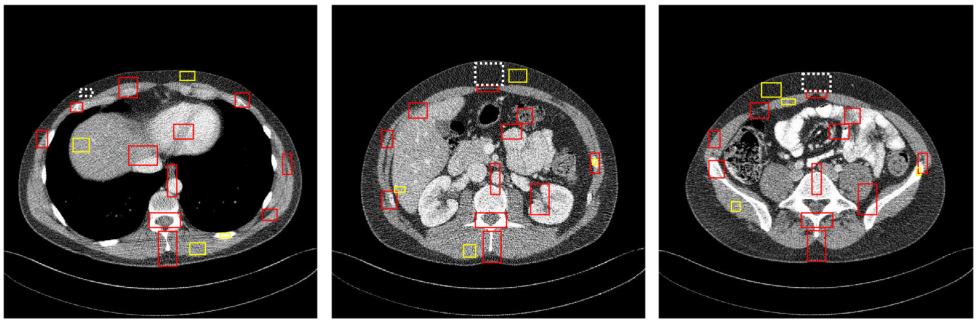

(**a**) LDCT image 1 (**b**) LDCT image 2 (**c**) LDCT image 3

Figure 5. ROIs considered to compute CNR and ENL measures.

For the setting of the method parameters, the PSNR measure has been studied as a function of them. In [19], authors observed that sub-optimal performance for the FRF-FPGA method in terms of PSNR can be obtained for th_1, th_2, and th_3 as a function of the rates of noise p and σ. The experiments show that for $\sigma \in [0, 40]$ and $p \in [0,\ 0.4]$, sub-optimal performance can be achieved by setting th_1, th_2, and th_3 as a function of σ and p, as shown in Equation (17):

$$\begin{aligned} th_1 &= 0.90 + \frac{\beta_{p,\sigma}}{0.4} 0.07, \\ th_2 &= 0.87 + \frac{\beta_{p,\sigma}}{0.4} 0.06, \\ th_3 &= 0.97 + \frac{\beta_{p,\sigma}}{0.4} 0.01, \end{aligned} \tag{17}$$

where $\beta_{p,\sigma} = p - 2\sigma/100$ depend on σ, the Gaussian noise standard deviation, and the impulsive noise p. There are different methodologies to estimate p and σ. In the experiments with LDCT images, where the noise distribution changes according to the dosage level, p was estimated using the methodology utilized in [42], and the estimation for σ was obtained using the technique presented in [43]. Therefore, utilizing these estimations for σ

and p, the parameters th_1, th_2, and th_3 were automatically set. The optimal setting depends on both noise and image characteristics. With this adjustment in our experimentation, we have achieved PSNR sub-optimal performance for all tested images.

Figures 6 and 7 present the dependence of the PSNR measure on the values F_σ and $\beta_{p,\sigma}$ for the Axial view image deteriorated with various rates of Gaussian-impulse noise. A similar performance is obtained for the other views, as shown in Figures 8 and 9, which present the dependence of the PSNR measure on the values F_σ and $\beta_{p,\sigma}$ for the Coronal view. Similar results were obtained for the Sagittal view. For noise intensities from 0% to 20%, the higher value of PSNR is obtained for $F_\sigma \in [50, 1500]$ and $\beta_{p,\sigma} \in [-0.6, 0.4]$. For noise intensities from 20% to 40%. the higher value of PSNR is obtained for $F_\sigma \in [250, 1500]$ and $\beta_{p,\sigma} \in [0.2, 0.6]$. Our experiments revealed that sub-optimal performance can be achieved by setting th_1, th_2, and th_3 as indicated in Equation (17).

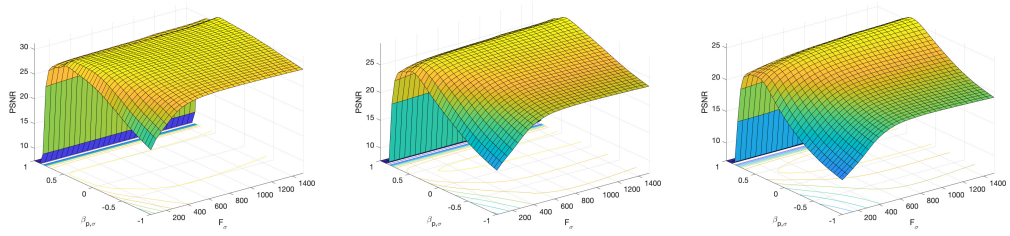

(**a**) (**b**) (**c**)

Figure 6. Dependence of the PSNR metric on the values F_σ and $\beta_{p,\sigma}$. Axial view corrupted with Gaussian σ and impulsive noise p. (**a**) $\sigma = 10$, $p = 0.1$. (**b**) $\sigma = 20$, $p = 0.2$. (**c**) $\sigma = 30$, $p = 0.3$.

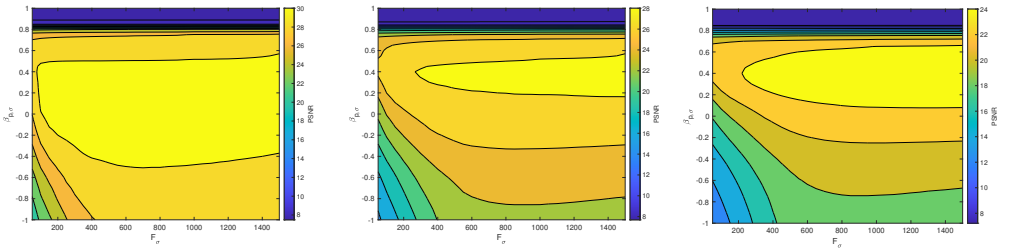

(**a**) (**b**) (**c**)

Figure 7. Surface plots for the dependence of the PSNR metric on the values F_σ and $\beta_{p,\sigma}$. Axial view corrupted with Gaussian σ and impulsive noise p. (**a**) $\sigma = 10$, $p = 0.1$. (**b**) $\sigma = 20$, $p = 0.2$. (**c**) $\sigma = 30$, $p = 0.3$.

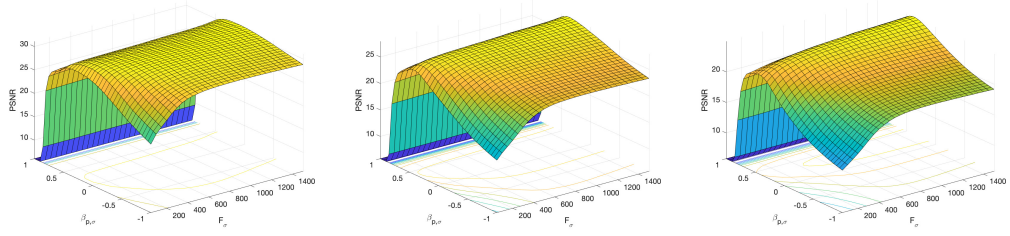

(**a**) (**b**) (**c**)

Figure 8. Dependence of the PSNR metric on the values F_σ and $\beta_{p,\sigma}$. Coronal view corrupted with Gaussian σ and impulsive noise p. (**a**) $\sigma = 10$, $p = 0.1$. (**b**) $\sigma = 20$, $p = 0.2$. (**c**) $\sigma = 30$, $p = 0.3$.

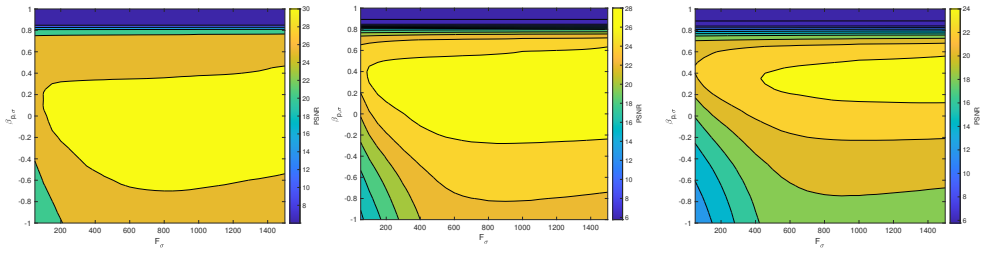

(**a**) (**b**) (**c**)

Figure 9. Surface plots for the dependence of the PSNR metric on the values F_σ and $\beta_{p,\sigma}$. Coronal view corrupted with Gaussian σ and impulsive noise p. (**a**) $\sigma = 10$, $p = 0.1$. (**b**) $\sigma = 20$, $p = 0.2$. (**c**) $\sigma = 30$, $p = 0.3$.

We studied the effect of the processing window dimension n and the α, α' values on PSNR value. The experiments indicated that the optimal values of the parameters n, α, and α' correspond with those obtained in our former analysis [19]. Consequently, in this experimentation, we have used 3×3 processing windows ($n = 3$) and $\alpha = 3$, $\alpha' = 1$.

With respect to the visual appearance, by examining the denoised outputs in Figures 10–13, we observe that the proposed filter satisfactorily preserves the details of the images and efficiently reduces the Gaussian-impulsive noise.

We compare the proposed algorithm with other competitive filters expressly designed to eliminate Gaussian-impulsive mixed noise that have been used successfully in medical image processing: the SFMR filter [44,45], the RLSF filter [46], and the FPGA filter [20,47]. These methods have been coded using the corresponding optimal parameters indicated by the authors.

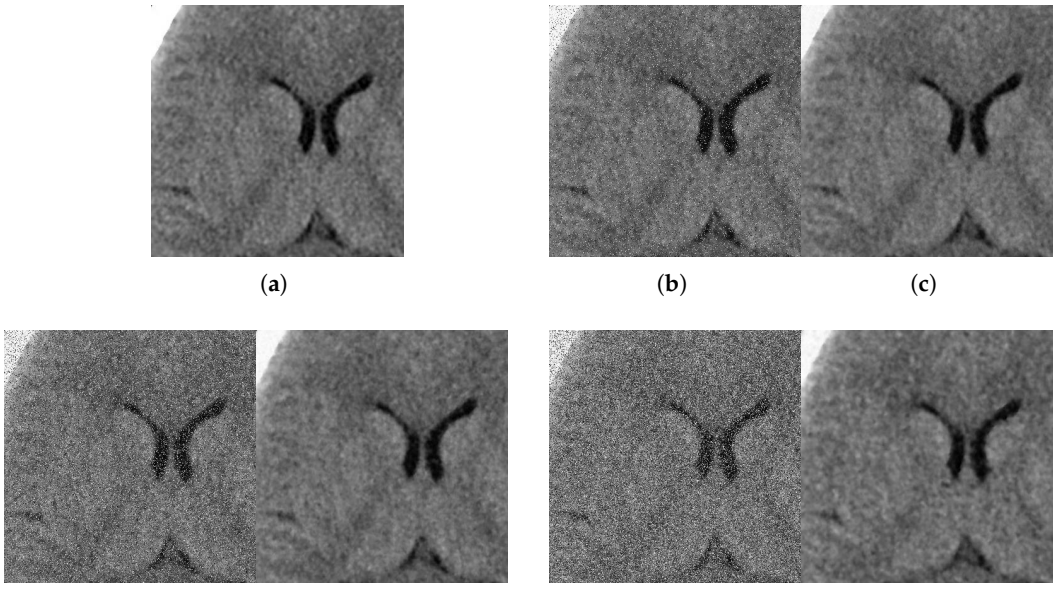

(**a**) (**b**) (**c**)

(**d**) (**e**) (**f**) (**g**)

Figure 10. Method outputs. Axial view corrupted with impulsive noise p and Gaussian σ. (**a**) Original axial. (**b**) Noisy $p = 0.1$, $\sigma = 10$. (**c**) Method output. (**d**) Noisy $p = 0.2$, $\sigma = 20$. (**e**) Method output. (**f**) Noisy $p = 0.3$, $\sigma = 30$. (**g**) Method output.

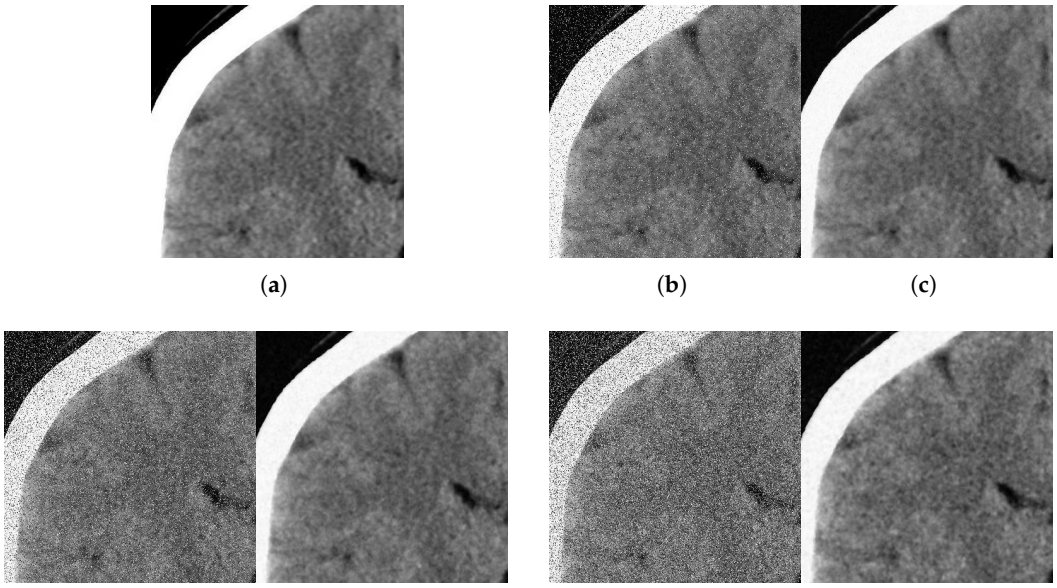

(**a**) (**b**) (**c**) (**d**) (**e**) (**f**) (**g**)

Figure 11. Method outputs. Coronal view corrupted with impulsive noise p and Gaussian σ. (**a**) Original coronal. (**b**) Noisy $p = 0.1$, $\sigma = 10$. (**c**) Method output. (**d**) Noisy $p = 0.2$, $\sigma = 20$. (**e**) Method output. (**f**) Noisy $p = 0.3$, $\sigma = 30$. (**g**) Method output.

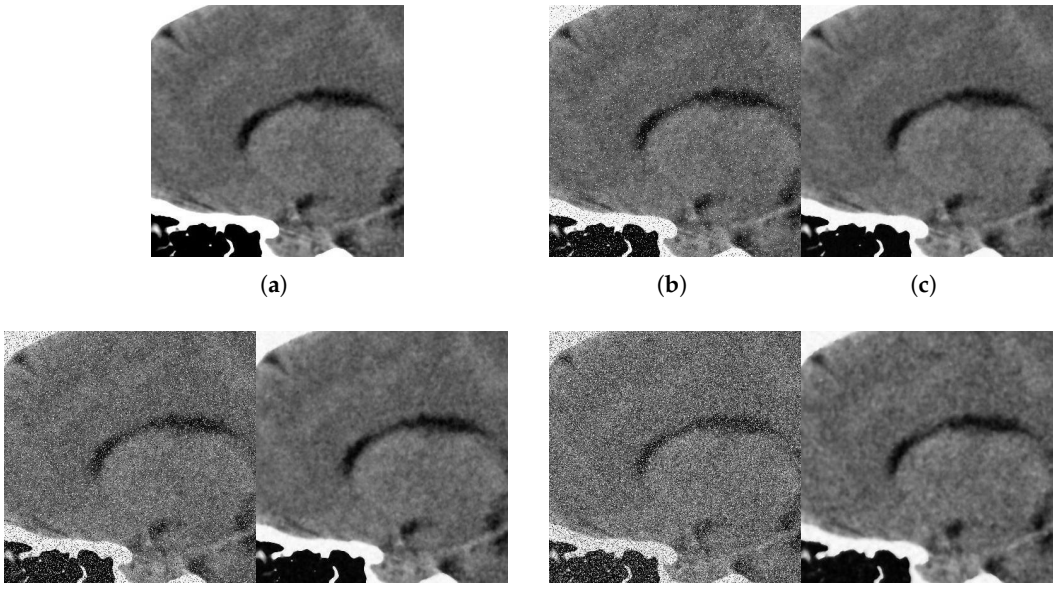

(**a**) (**b**) (**c**) (**d**) (**e**) (**f**) (**g**)

Figure 12. Method outputs. Sagittal view corrupted with impulsive noise p and Gaussian σ. (**a**) Original sagittal. (**b**) Noisy $p = 0.1$, $\sigma = 10$. (**c**) Method output. (**d**) Noisy $p = 0.2$, $\sigma = 20$. (**e**) Method output. (**f**) Noisy $p = 0.3$, $\sigma = 30$. (**g**) Method output.

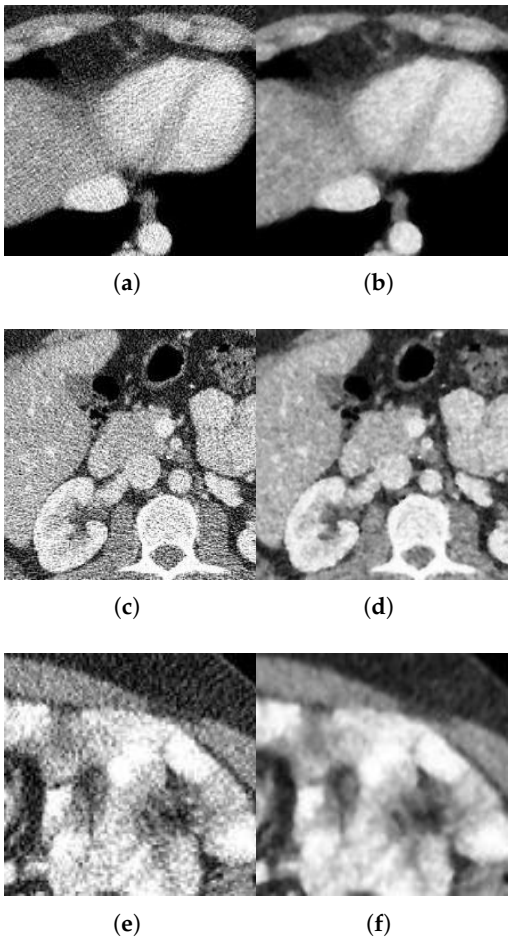

Figure 13. Method outputs for LDCT abdominal images. (**a**) Quater-dose LDCT image 1. (**b**) Method output. (**c**) Quater-dose LDCT image 2. (**d**) Method output. (**e**) Quater-dose LDCT image 3. (**f**) Method output.

Tables 1–4 present the MAE, PSNR, MSSIM, and IEF measures for the brain CT images corrupted with various rates of impulsive and Gaussian noise. These experiments show that the introduced algorithm exhibits the best performance in all results in terms of the MAE, PSNR, SSIM, and IEF metrics. This implicates that the proposed filter exhibits a better noise removal and better preserves the image details. Table 5 shows the SNR, CNR, and ENL image quality values for the original and denoised abdominal LDCT images. From Table 5, it can be seen that the proposed filter outperforms all the compared methods (RLSF, SFRF, and FPGA) by achieving the highest values in SNR, CNR, and ENL. The proposed method is 12.9–14.2 dB higher than the noisy original image on average in the SNR value and increases the value of structural protection by 13.1–15.0 dB higher than the noisy original image on average in the CNR value. Moreover, the ENL value is 2.3–3 times higher than the original image. Obtained values for these objective metrics indicate that the filter exhibits a robust performance.

Table 1. MAE measure for noisy and denoised CT images. Values in bold denote the best filtering quality.

Noise		MAE				
Gaussian	**Impulsive**	**Noisy**	**RLSF**	**SFRF**	**FPGA**	**New Filter**
Axial view						
$\sigma = 10$	$p = 0.1$	19.23	8.31	5.78	6.29	**5.47**
$\sigma = 20$	$p = 0.2$	31.83	13.99	9.27	9.30	**6.59**
$\sigma = 30$	$p = 0.3$	44.20	21.23	13.95	16.41	**8.18**
Coronal view						
$\sigma = 10$	$p = 0.1$	18.62	8.55	5.93	5.82	**5.34**
$\sigma = 20$	$p = 0.2$	31.68	14.03	9.41	9.54	**7.15**
$\sigma = 30$	$p = 0.3$	44.04	21.07	14.10	16.73	**9.22**
Sagittal view						
$\sigma = 10$	$p = 0.1$	18.85	8.82	5.93	5.80	**5.44**
$\sigma = 20$	$p = 0.2$	32.12	14.85	9.54	9.61	**6.94**
$\sigma = 30$	$p = 0.3$	44.65	22.45	14.46	17.11	**8.61**

Table 2. PSNR measure for noisy and denoised CT images. Values in bold denote the best filtering quality.

Noise		PSNR				
Gaussian	**Impulsive**	**Noisy**	**RLSF**	**SFRF**	**FPGA**	**New Filter**
Axial view						
$\sigma = 10$	$p = 0.1$	15.82	28.08	30.89	29.75	**31.30**
$\sigma = 20$	$p = 0.2$	12.87	23.60	27.22	26.36	**29.58**
$\sigma = 30$	$p = 0.3$	11.13	19.95	23.74	21.28	**27.35**
Coronal view						
$\sigma = 10$	$p = 0.1$	15.99	27.20	29.88	29.17	**31.11**
$\sigma = 20$	$p = 0.2$	12.97	23.28	26.56	25.68	**28.22**
$\sigma = 30$	$p = 0.3$	11.17	19.86	23.30	20.95	**26.17**
Sagittal view						
$\sigma = 10$	$p = 0.1$	15.71	27.23	30.24	29.78	**31.16**
$\sigma = 20$	$p = 0.2$	12.72	23.07	26.71	25.84	**28.54**
$\sigma = 30$	$p = 0.3$	10.93	19.59	23.33	20.70	**26.63**

Table 3. MSSIM measure for noisy and denoised CT images. Values in bold denote the best filtering quality.

Noise		MSSIM				
Gaussian	**Impulsive**	**Noisy**	**RLSF**	**SFRF**	**FPGA**	**New Filter**
Axial view						
$\sigma = 10$	$p = 0.1$	0.1077	0.5048	0.5499	0.5412	**0.5600**
$\sigma = 20$	$p = 0.2$	0.0534	0.4628	0.4769	0.4299	**0.5225**
$\sigma = 30$	$p = 0.3$	0.0345	0.4146	0.4405	0.2716	**0.4816**
Coronal view						
$\sigma = 10$	$p = 0.1$	0.1349	0.6098	0.6469	0.6531	**0.6532**
$\sigma = 20$	$p = 0.2$	0.0709	0.5623	0.5794	0.5119	**0.6036**
$\sigma = 30$	$p = 0.3$	0.0472	0.5002	0.5421	0.3241	**0.5441**
Sagittal view						
$\sigma = 10$	$p = 0.1$	0.1113	0.4919	0.5429	0.5534	**0.5545**
$\sigma = 20$	$p = 0.2$	0.0583	0.4463	0.4703	0.4179	**0.5063**
$\sigma = 30$	$p = 0.3$	0.0390	0.3977	0.4345	0.2619	**0.4678**

For small values of σ and p, the FPGA obtains similar results of MSSIM to the new method. However, for large values of noise, the proposed filter outperforms all the other filters.

Table 4. IEF measure for noisy and filtered images. Values in bold denote the best filtering quality.

Noise		IEF				
Gaussian	**Impulsive**	**Noisy**	**RLSF**	**SFRF**	**FPGA**	**New Filter**
Axial view						
$\sigma = 10$	$p = 0.1$	1	16.84	32.15	25.28	**35.36**
$\sigma = 20$	$p = 0.2$	1	11.83	27.23	22.84	**46.60**
$\sigma = 30$	$p = 0.3$	1	7.71	18.45	10.48	**42.38**
Coronal view						
$\sigma = 10$	$p = 0.1$	1	13.21	24.48	20.77	**32.49**
$\sigma = 20$	$p = 0.2$	1	10.73	22.84	18.66	**33.30**
$\sigma = 30$	$p = 0.3$	1	7.40	16.33	9.51	**31.60**
Sagittal view						
$\sigma = 10$	$p = 0.1$	1	14.18	28.38	25.51	**35.08**
$\sigma = 20$	$p = 0.2$	1	10.84	25.09	20.53	**38.18**
$\sigma = 30$	$p = 0.3$	1	7.33	17.36	9.49	**37.11**

Table 5. SNR, ENL, and CNR measures for noisy low-dose CT images. Values in bold denote the best filtering quality.

Method	**SNR (dB)**	**CNR (dB)**	**ENL**
LDCT image 1			
Noisy	22.9282	8.2222	10.0281
RLSF	33.3576	18.6606	21.0721
SFRF	34.9700	20.6087	22.8512
FPGA	34.5917	19.8566	22.1175
New filter	**35.9049**	**21.4057**	**23.6885**
LDCT image 2			
Noisy	20.4850	6.0844	5.2926
RLSF	32.7105	19.6692	14.2302
SFRF	33.9070	20.5045	15.7191
FPGA	33.6989	19.9728	15.2304
New filter	**34.1144**	**21.0848**	**16.1316**
LDCT image 3			
Noisy	20.6764	6.4583	6.0984
RLSF	31.3755	17.6572	13.4903
SFRF	33.6482	19.1170	15.0607
FPGA	33.0195	18.9262	14.2957
New filter	**34.9407**	**20.4838**	**15.9328**

3.2. Computational Efficiency

We have coded a parallel implementation for shared memory parallel computers with OpenMP [28,29]. OpenMP software is an application programming interface (API) addressed to shared memory parallel computing in different programming languages (C, C++, and Fortran), available for the majority of operating systems and platforms. We developed the experiments on a shared memory parallel machine: a multi-core platform equipped with two Intel(R) Xeon(R) Gold 6140 CPU, 2.30 GHz with 24.75 MB L3 Cache. Each processor is composed of 18 physical cores, resulting in a total number of 36 cores in the computer. The main memory size is 384 GB of DDR3. Both the parallel and serial code were developed using the GNU gcc-11.1.0 compiler. Table 6 presents the computational

time in seconds using the 36 cores of the parallel machine. It can be observed that there is not a significant dependence of the time on the amount of noise. This fact is due to the characteristics of the filter. To study the efficiency of the parallel OpenMP implementation, we carry out the experimentation by increasing the amount of computing units. Figure 14 presents the speed-up obtained by the parallel implementation for the Sagittal view image contaminated with $\sigma = 30$ Gaussian noise and $p = 0.3$ impulsive noise. Similar results in speed-up were achieved for all the tested images. The results show that a substantial speed-up is achieved. The experiments show that the parallel implementation obtains speed-ups in the range of 25.54 to 28.24 when the 36 computing units of the multi-core were utilized. The number of computing units in the employed machine is 36. If a machine with greater number of computing elements was used, a greater speed-up would be obtained. Similar conclusions were obtained for the other CT images. The times presented in Table 6 show that the proposed algorithm enables the filtering of large CT medical images in reduced times, which makes the method appropriate for real scenarios.

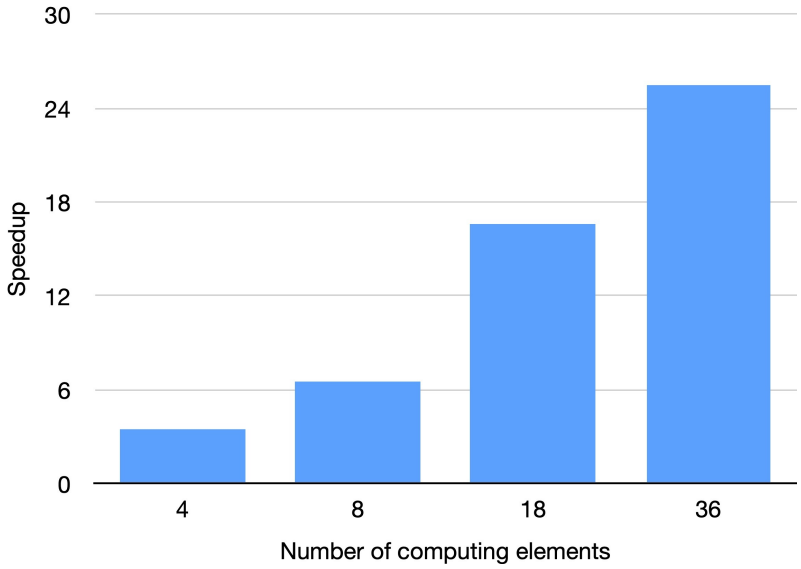

Figure 14. Speed-up for parallel implementation. Sagittal view corrupted with $\sigma = 30$, $p = 0.3$.

Table 6. Computational time.

Noise		**Time (seconds)**		
Brain CT images				
Gaussian Noise	Impulsive Noise	Axial view	Coronal view	Sagittal view
$\sigma = 10$	$p = 0.1$	0.0873	0.0870	0.0793
$\sigma = 20$	$p = 0.2$	0.0877	0.0871	0.0811
$\sigma = 30$	$p = 0.3$	0.0886	0.0885	0.0813
Low-dose abdominal CT images				
Images obtained with quarter-dose exposure		LDCT 1	LDCT 2	LDCT 2
		0.0429	0.0460	0.0405

4. Conclusions

An efficient parallel algorithm based on fuzzy logic has been introduced to remove Gaussian-impulsive noise in CT medical images. The filter has been implemented on shared memory parallel machines utilizing OpenMP. The implementation has been utilized to remove Gaussian-impulsive mixed noise on medical CT images corrupted with different noise levels. A comparison analysis with state-of-the-art denoising methods is performed using qualitative and quantitative measures (PSNR, MAE, IEF, MSSIM, SNR, CNR, and

ENL) and demonstrating the competitiveness of the proposed technique. The parallel algorithm introduced exhibited reduced computing times making the proposed technique applicable for real-time medical image filtering. In future studies, we will study the use of this methodology to remove other kinds of noise in medical images from US, PET, and MRI. Moreover, we will implement the algorithm on GPUs making use of CUDA.

Author Contributions: Writing—original draft preparation, J.A. and L.S.; supervision, J.A.; funding acquisition, J.A.; conceptualization, J.A. and L.S.; methodology, L.S. and J.A.; writing—review and editing, J.A.; software, L.S.; validation, J.A.; investigation, J.A. and L.S.; resources, J.A. All authors have read and agreed to the published version of the manuscript.

Funding: This research was funded by the Spanish Ministry of Science, Innovation and Universities (Grant RTI2018-098156-B-C54), and it was co-financed with FEDER funds.

Data Availability Statement: Not applicable.

Acknowledgments: The authors would like to thank the editor and reviewers for their comments and suggestions which helped to improve the quality of the paper significantly.

Conflicts of Interest: The authors declare no conflict of interest.

References

1. Kalra, M.K.; Wittram, C.; Maher, M.M.; Sharma, A.; Avinash, G.B.; Karau, K.; Toth, T.L.; Halpern, E.; Saini, S.; Shepard, J.A. Can Noise Reduction Filters Improve Low-Radiation-Dose Chest CT Images Pilot Study. *Radiology* **2003**, *228*, 257–264. [CrossRef]
2. Kalra, M.K.; Maher, M.M.; Blake, M.A.; Lucey, B.C.; Karau, K.; Toth, T.L.; Avinash, G.; Halpern, E.F.; Saini, S. Detection and Characterization of Lesions on Low-Radiation-Dose Abdominal CT Images Postprocessed with Noise Reduction Filters. *Radiology* **2004**, *232*, 791–797. [CrossRef]
3. Kumar, M.; Tounsi, Y.; Kaur, K.; Nassim, A.; Mandoza-Santoyo, F.; Matoba, O. Speckle denoising techniques in imaging systems. *J. Opt.* **2020**, *22*, 063001. [CrossRef]
4. Plataniotis, K.; Venetsanopoulos, A.N. *Color Image Processing and Applications*; Springer: Berlin/Heidelberg, Germany, 2013.
5. Boncelet, C. 4.5—Image Noise Models. In *Handbook of Image and Video Processing*, 2nd ed.; Bovik, A., Ed.; Communications, Networking and Multimedia; Academic Press: Burlington, MA, USA, 2005; pp. 397–409.
6. Lin, M.H.; Hou, Z.X.; Cheng, K.H.; Wu, C.H.; Peng, Y.T. Image Denoising Using Adaptive and Overlapped Average Filtering and Mixed-Pooling Attention Refinement Networks. *Mathematics* **2021**, *9*, 1130. [CrossRef]
7. Radlak, K.; Malinski, L.; Smolka, B. Deep Learning Based Switching Filter for Impulsive Noise Removal in Color Images. *Sensors* **2020**, *20*, 2782. [CrossRef] [PubMed]
8. Smolka, B. Peer group switching filter for impulse noise reduction in color images. *Pattern Recognit. Lett.* **2010**, *31*, 484–495. [CrossRef]
9. Camarena, J.G.; Gregori, V.; Morillas, S.; Sapena, A. Fast detection and removal of impulsive noise using peer groups and fuzzy metrics. *J. Vis. Commun. Image Represent.* **2008**, *19*, 20–29. [CrossRef]
10. Toprak, A.; Güler, I. Impulse noise reduction in medical images with the use of switch mode fuzzy adaptive median filter. *Digit. Signal Process.* **2007**, *17*, 711–723. [CrossRef]
11. Schulte, S.; Nachtegael, M.; Witte, V.D.; der Weken, D.V.; Kerre, E.E. A fuzzy impulse noise detection and reduction method. *IEEE Trans. Image Process.* **2006**, *15*, 1153–1162. [CrossRef]
12. Schulte, S.; Morillas, S.; Gregori, V.; Kerre, E.E. A New Fuzzy Color Correlated Impulse Noise Reduction Method. *IEEE Trans. Image Process.* **2007**, *16*, 2565–2575. [CrossRef] [PubMed]
13. Mélange, T.; Nachtegael, M.; Kerre, E.E. Fuzzy Random Impulse Noise Removal From Color Image Sequences. *IEEE Trans. Image Process.* **2011**, *20*, 20–22. [CrossRef]
14. Camarena, J.G.; Gregori, V.; Morillas, S.; Sapena, A. Two-step fuzzy logic-based method for impulse noise detection in colour images. *Pattern Recognit. Lett.* **2010**, *31*, 1842–1849. [CrossRef]
15. Tomasi, C.; Manduchi, R. Bilateral filtering for gray and color images. In Proceedings of the Sixth International Conference on Computer Vision (IEEE Cat. No.98CH36271), Bombay, India, 4–7 January 1998; IEEE Computer Society: Washington, DC, USA, 1998; pp. 839–846.
16. Li, X. On modeling interchannel dependency for color image denoising. *Int. J. Imaging Syst. Technol.* **2007**, *17*, 163–173. [CrossRef]
17. Dabov, K.; Foi, A.; Katkovnik, V.; Egiazarian, K. Image Denoising by Sparse 3-D Transform-Domain Collaborative Filtering. *Trans. Img. Proc.* **2007**, *16*, 2080–2095. [CrossRef]
18. Kong, X.; Zhao, Y.; Xue, J.; Chan, J.C.W. Hyperspectral Image Denoising Using Global Weighted Tensor Norm Minimum and Nonlocal Low-Rank Approximation. *Remote Sens.* **2019**, *11*, 2281. [CrossRef]
19. Arnal, J.; Súcar, L. Hybrid Filter Based on Fuzzy Techniques for Mixed Noise Reduction in Color Images. *Appl. Sci.* **2020**, *10*, 243. [CrossRef]

20. Morillas, S.; Gregori, V.; Hervás, A. Fuzzy peer groups for reducing mixed Gaussian-impulse noise from color images. *IEEE Trans. Image Process.* **2009**, *18*, 1452–1466. [CrossRef] [PubMed]
21. Xiao, G.; Li, K.; Li, K. Reporting l most influential objects in uncertain databases based on probabilistic reverse top-k queries. *Inf. Sci.* **2017**, *405*, 207–226. [CrossRef]
22. Xiao, G.; Li, K.; Li, K.; Zhou, X. Efficient top-(k, l) range query processing for uncertain data based on multicore architectures. *Distrib. Parallel Databases* **2015**, *33*, 381–413. [CrossRef]
23. Xiao, G.; Li, K.; Li, K. Reporting l most favorite objects in uncertain databases with probabilistic reverse top-k queries. In Proceedings of the 2015 IEEE International Conference on Data Mining Workshop (ICDMW), Atlantic City, NJ, USA, 14–17 November 2015; pp. 1592–1599.
24. Chen, Y.; Li, K.; Yang, W.; Xiao, G.; Xie, X.; Li, T. Performance-Aware Model for Sparse Matrix-Matrix Multiplication on the Sunway TaihuLight Supercomputer. *IEEE Trans. Parallel Distrib. Syst.* **2018**, *30*, 923–938. [CrossRef]
25. Liu, C.; Li, K.; Xu, C.; Li, K. Strategy Configurations of Multiple Users Competition for Cloud Service Reservation. *IEEE Trans. Parallel Distrib. Syst.* **2016**, *27*, 508–520. [CrossRef]
26. Li, K.; Liu, C.; Li, K.; Zomaya, A.Y. A framework of price bidding configurations for resource usage in cloud computing. *IEEE Trans. Parallel Distrib. Syst.* **2016**, *27*, 2168–2181. [CrossRef]
27. Wong, K.K.; Fong, S.; Wang, D. Impact of advanced parallel or cloud computing technologies for image guided diagnosis and therapy. *J. X-Ray Sci. Technol.* **2017**, *25*, 187–192. [CrossRef]
28. Dagum, L.; Menon, R. OpenMP: An industry standard API for shared-memory programming. *IEEE Comput. Sci. Eng.* **1998**, *5*, 46–55. [CrossRef]
29. OpenMP ARB. Available online: https://www.openmp.org (accessed on 8 September 2022).
30. McCollough, C.; Chen, B.; Holmes, D.; Duan, X.; Yu, Z.; Xu, L.; Leng, S.; Fletcher, J. Low dose CT image and projection data (LDCT-and-Projection-data) (Version 4). *Med. Phys.* **2021**, *48*, 902–911. [CrossRef]
31. Coupé, P.; Yger, P.; Prima, S.; Hellier, P.; Kervrann, C.; Barillot, C. An optimized blockwise nonlocal means denoising filter for 3-D magnetic resonance images. *IEEE Trans. Med. Imag.* **2008**, *27*, 425–441. [CrossRef]
32. Wang, Z.; Bovik, A.C.; Sheikh, H.R.; Simoncelli, E.P. Image quality assessment: From error visibility to structural similarity. *IEEE Trans. Image Process.* **2004**, *13*, 600–612. [CrossRef]
33. Arnal, J.; Mayzel, I. Parallel techniques for speckle noise reduction in medical ultrasound images. *Adv. Eng. Softw.* **2020**, *148*, 102867. [CrossRef]
34. Adler, D.C.; Ko, T.H.; Fujimoto, J.G. Speckle reduction in optical coherence tomography images by use of a spatially adaptive wavelet filter. *Opt. Lett.* **2004**, *29*, 2878–2880. [CrossRef] [PubMed]
35. Garnett, R.; Huegerich, T.; Chui, C.; He, W. A universal noise removal algorithm with an impulse detector. *IEEE Trans. Image Process.* **2005**, *14*, 1747–1754. [CrossRef] [PubMed]
36. Morillas, S.; Gregori, V.; Peris-Fajarnés, G.; Latorre, P. A fast impulsive noise color image filter using fuzzy metrics. *Real-Time Imaging* **2005**, *11*, 417–428. [CrossRef]
37. Lukac, R.; Plataniotis, K.N. A Taxonomy of Color Image Filtering and Enhancement Solutions. *Adv. Imaging Electron. Phys.* **2006**, *140*, 187–264.
38. Kenney, C.; Deng, Y.; Manjunath, B.S.; Hewer, G. Peer group image enhancement. *IEEE Trans. Image Process.* **2001**, *10*, 326–334. [CrossRef]
39. Gregori, V.; Miñana, J.J.; Sapena, A. Completable fuzzy metric spaces. *Topol. Appl.* **2017**, *225*, 103–111. [CrossRef]
40. Morillas, S.; Gregori, V.; Peris-Fajarnés, G. Isolating impulsive noise pixels in color images by peer group techniques. *Comput. Vis. Image Underst.* **2008**, *110*, 102–116. [CrossRef]
41. Esakkirajan, S.; Veerakumar, T.; Subramanyam, A.N.; PremChand, C. Removal of high density salt and pepper noise through modified decision based unsymmetric trimmed median filter. *IEEE Signal Process. Lett.* **2011**, *18*, 287–290. [CrossRef]
42. Smolka, B.; Plataniotis, K.N.; Chydzinski, A.; Szczepanski, M.; Venetsanopoulos, A.N.; Wojciechowski, K. Self-adaptive algorithm of impulsive noise reduction in color images. *Pattern Recognit.* **2002**, *35*, 1771–1784. [CrossRef]
43. Shin, D.H.; Park, R.H.; Yang, S.; Jung, J.H. Block-based noise estimation using adaptive Gaussian filtering. *IEEE Trans. Consum. Electron.* **2005**, *51*, 218–226. [CrossRef]
44. Camarena, J.G.; Gregori, V.; Morillas, S.; Sapena, A. A simple fuzzy method to remove mixed Gaussian-impulsive noise from color images. *IEEE Trans. Fuzzy Syst.* **2013**, *21*, 971–978. [CrossRef]
45. Arnal, J.; Pérez, J.B.; Vidal, V. A Parallel Fuzzy Method to Reduce Mixed Gaussian-Impulsive Noise in CT Medical Images. In Proceedings of the International Conference on Natural Computation, Fuzzy Systems and Knowledge Discovery, Kunming, China, 20–22 July 2019; Springer: Cham, Switzerland, 2019; pp. 975–982.
46. Smolka, B.; Kusnik, D. Robust local similarity filter for the reduction of mixed Gaussian and impulsive noise in color digital images. *Signal Image Video Process.* **2015**, *9*, 49–56. [CrossRef]
47. Arnal, J.; Chillarón, M.; Parcero, E.; Súcar, L.B.; Vidal, V. A parallel fuzzy algorithm for real-time medical image enhancement. *Int. J. Fuzzy Syst.* **2020**, *22*, 2599–2612. [CrossRef]